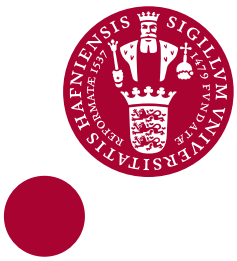

Sensitivity-enhanced quadrupolar-echo NMR of half-integer quadrupolar nuclei. Magnitudes and relative orientation of chemical shielding and quadrupolar coupling tensors.

Larsen, Flemming Hofmann; Jakobsen, Hans J.; Nielsen, Niels Chr.

Published in:
Journal of the American Chemical Society

Publication date:
1997

Document version
Early version, also known as pre-print

Sensitivity-Enhanced Quadrupolar-Echo NMR of Half-Integer Quadrupolar Nuclei. Magnitudes and Relative Orientation of Chemical Shielding and Quadrupolar Coupling Tensors

Flemming H. Larsen,[†] Hans J. Jakobsen,[†] Paul D. Ellis,[‡] and Niels Chr. Nielsen*[,†]

Instrument Centre for Solid-State NMR Spectroscopy, Department of Chemistry, University of Aarhus, DK-8000 Aarhus C, Denmark, and Environmental Molecular Sciences Laboratory, Pacific Northwest National Laboratory, Richland, Washington 99352

Received: May 8, 1997; In Final Form: September 15, 1997[⊗]

A novel approach to quadrupolar-echo (QE) NMR of half-integer quadrupolar nuclei in static powders is analyzed. By acquisition of the QE spectrum during a Carr−Purcell−Meiboom−Gill (CPMG) train of selective π pulses, the second-order quadrupolar line shape for the central transition is split into a comb of sidebands leading to a considerable increase in the sensitivity compared to a conventional QE spectrum. The applicability of the method for determination of magnitudes and relative orientation of chemical shielding and quadrupolar coupling tensors is examined. Through numerical simulation and iterative fitting of experimental ^{87}Rb ($RbClO_4$ and $RbVO_3$) and ^{59}Co spectra ($Co(NH_3)_5\ Cl_3$), it is demonstrated that the quadrupolar CPMG experiment represents a useful method for studying half-integer quadrupolar nuclei exhibiting large quadrupolar coupling combined with anisotropic chemical shielding interactions. Sensitivity enhancements by a factor of up to about 30 are observed for the samples studied.

1. Introduction

The quadrupolar-echo (QE) solid-state NMR experiment[1−3] is among one of the most widely used experiments for studying quadrupolar nuclei in powder samples. Through its ability to detect rapidly decaying free induction decays outside the period of receiver dead time and probe ringing using a spin−echo,[1,4] variants of the QE experiment have been used extensively for studying local electric field gradients or molecular dynamics of integer (e.g., ^{2}H)[5−11] as well as half-integer quadrupolar nuclei[12−16] in a variety of amorphous and polycrystalline solids. Although QE spectra for integer quadrupolar nuclei are typically dominated by large first-order quadrupolar coupling effects, the QE spectra of half-integer quadrupolar nuclei may provide simultaneous information about several anisotropic interactions. This is ascribed to the fact that QE spectra for half-integer quadrupolar nuclei may be tuned to selectively observe the (1/2, −1/2) central transition, which is perturbed by the quadrupolar interaction only to second order and thereby also allows detection of effects from other less dominant anisotropic interactions. Among these interactions the anisotropic chemical shielding should be mentioned in particular. Since the magnitudes and relative orientation of quadrupolar and chemical shielding tensors may provide detailed information about the electronic environment of the nucleus, the QE experiment has recently attracted considerable attention as a tool for retrieving information about these interactions for powder samples.[12−16]

When using QE NMR as a probe to obtain information on magnitudes and relative orientation of quadrupolar and chemical shielding tensors, one may be faced with two problems. First, for large anisotropic interactions (e.g., quadrupole couplings in the range 5−30 MHz) the central transition line shape may extend over hundreds of kilohertz, leading to low sensitivity. Second, when the magnitudes of the anisotropic interactions become large relative to the amplitude of the rf irradiation field, the excitation profile of the rf pulse becomes anisotropic (i.e., dependent on the orientation of the crystallite), which must be taken into account in the determination of the anisotropic interactions from experimental spectra.

It is well-known that spin−echo methods such as those in the Carr−Purcell[17] and Carr−Purcell−Meiboom−Gill (CPMG)[18] experiments enable efficient separation of inhomogeneous and homogeneous (in the sense of Maricq and Waugh[19]) NMR interactions.[20−25] So far, this feature has primarily been used to obtain information about homonuclear dipolar couplings[20,24,26] and molecular dynamics[21−23,25,27−30] (both behaving as homogeneous interactions) either by just measuring the points constituting the echo maxima or by measuring the full envelopes of the spin−echoes. In the former case, the inhomogeneous interactions are refocused, implying that the spectra primarily probe the homogeneous interactions. In the latter case, the Fourier transformed spectrum consists of a sideband manifold from which information about *both* homogeneous and inhomogeneous interactions may be extracted. The homogeneous interactions affect the line shape of the sidebands, whereas information about the inhomogeneous interactions may be extracted from the envelope of the sideband manifold.

Obviously, the utility of spin−echo multiple-pulse experiments is not restricted to the determination of homogeneous interactions. In this work we examine the quadrupolar version of the CPMG experiment (previously referred to as quadrupolar CPMG[23] and spikelet[29]) with respect to sensitivity enhancement of QE spectra for half-integer quadrupolar nuclei recorded with the aim of determining parameters for the inhomogeneous interactions. In particular, the quadrupolar CPMG experiment is analyzed for the purpose of determination of magnitudes and relative orientation of quadrupolar coupling and anisotropic chemical shielding tensors for half-integer quadrupolar nuclei (^{87} Rb and ^{59}Co) exhibiting very large quadrupolar coupling constants. For this purpose, the experiment is described theoretically using average Hamiltonian theory to second order. This theory forms the basis for a computer simulation program that allows iterative fitting of experimental spectra under conditions of ideal as well as nonideal (finite) rf pulse conditions. The method is demonstrated theoretically and

* To whom correspondence should be addressed. Fax: +45 86196199. Telephone: +45 89423841. E-mail: ncn@kemi.aau.dk.
[†] University of Aarhus.
[‡] Pacific Northwest National Laboratory.
[⊗] Abstract published in *Advance ACS Abstracts,* November 1, 1997.

S1089-5639(97)01547-8 CCC: $14.00

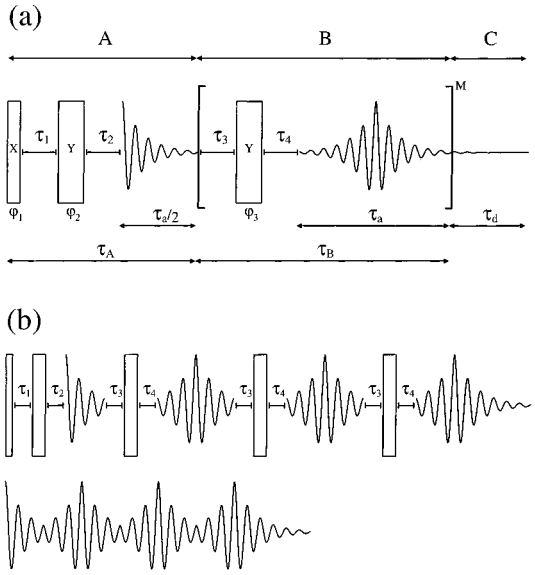

Figure 1. Quadrupolar CPMG (QCPMG) pulse sequence for sensitivity-enhanced quadrupolar-echo (QE) solid-state NMR of half-integer quadrupolar nuclei: (a) timing scheme of the pulse sequence; (b) relation between the pulse sequence timing t and the timing t_2 of the free induction decay (see text). Shaded and open bars correspond to selective (central transition) $\pi/2$ and π pulses, respectively. The phases ϕ_1, ϕ_2, ϕ_3, and the receiver reference phase ϕ_{rec} are cycled (see Table 2) to select the $p = 0 \rightarrow \pm1 \rightarrow \mp1 \rightarrow \pm1$ etc. coherence transfer pathways.

experimentally with examples from ^{87}Rb and ^{59}Co spectra of inorganic salts.

2. Theory

The quadrupolar CPMG (henceforth referred to as QCPMG) pulse sequence proposed for sensitivity-enhanced QE NMR of half-integer quadrupolar nuclei is depicted in Figure 1a. The pulse sequence consists of three parts. Part A is a standard QE sequence with τ_2 optimized such that the acquisition starts at the echo maximum. The repeating unit in part B accomplishes sampling of the spin−echoes generated by the interrupting train of π_y refocusing pulses. The receiver-off periods τ_3 and τ_4 bracketing the refocusing pulses serve to protect the receiver from the effects of the π_y pulses. Finally, part C extends the decaying part of the final spin−echo to the free induction decay (FID) to avoid undesired baseline problems and sinc wiggles upon Fourier transformation. It is noted that the flip angles of all pulses correspond to the angles effective for selective operation on the (−1/2, 1/2) central transition. Thus, in practical implementations for half-integer spin-I quadrupolar nuclei the flip angles should be reduced by a factor $(I + 1/2)$ in the limit of large quadrupole coupling constants.[31,32]

In the usual Zeeman interaction representation, the evolution of the spin states for an ensemble of quadrupolar nuclei may to a good approximation be described by the high-field truncated average Hamiltonian (assuming $|H_Q| \gg |H_\sigma|$)

$$\bar{\tilde{H}} = \bar{\tilde{H}}^{(1)}_{\sigma} + \bar{\tilde{H}}^{(1)}_{Q} + \bar{\tilde{H}}^{(2)}_{Q} + H_{rf} \quad (1)$$

where $\bar{\tilde{H}}^{(1)}_{\sigma}$ includes the secular first-order terms of the anisotropic chemical shielding interaction, $\bar{\tilde{H}}^{(1)}_{\sigma}$ and $\bar{\tilde{H}}^{(2)}_{Q}$ the secular first- and second-order terms of the quadrupolar coupling, and H_{rf} the external perturbation by rf irradiation. The Hamiltonian for rf irradiation with amplitude $\omega_{rf} = -\gamma B_{rf}$ and phase ϕ is given by

$$H_{rf} = \omega_{rf}(I_x \cos\phi + I_y \sin\phi) \quad (2)$$

TABLE 1: Irreducible Tensor Operators for Chemical Shielding and Quadrupolar Coupling Interactions[a]

		chemical shielding		quadrupolar coupling	
j	m	$T^{\sigma}_{j,m}$	$(R^{\sigma}_{j,m})^P$	$T^{Q}_{j,m}$	$(R^{Q}_{j,m})^P$
0	0	I_z	σ_{iso}		
2	−2	0	$-\frac{\eta_\sigma}{2}\sigma_{aniso}$	$\frac{1}{2}I_-{}^2$	$-\frac{\eta_\sigma}{2}$
2	−1	$\frac{1}{2}I_-$	0	$\frac{1}{2}(I_-I_z + I_zI_-)$	0
2	0	$\sqrt{\frac{2}{3}}I_z$	$\sqrt{\frac{3}{2}}\sigma_{aniso}$	$\frac{1}{\sqrt{6}}(3I_z^2 - I(I+1))$	$\sqrt{\frac{3}{2}}$
2	1	$-\frac{1}{2}I^+$	0	$-\frac{1}{2}(I_+I_z + I_zI_+)$	0
2	2	0	$-\frac{\eta_\sigma}{2}\sigma_{aniso}$	$\frac{1}{2}I_+{}^2$	$-\frac{\eta_\sigma}{2}$

[a] The spatial tensor elements in the principal axis frame P are related to the principal elements of the anisotropic interaction (R_{xx}, R_{yy}, R_{zz}) according to $R_{iso} = (R_{xx} + R_{yy} + R_{zz})/3$, $R_{aniso} = R_{zz} - R_{iso}$, $\eta = (R_{yy} - R_{xx})/R_{aniso}$ using the ordering $|R_{zz} - R_{iso}| \geq |R_{xx} - R_{iso}| \geq |R_{yy} - R_{iso}|$.

while the secular Hamiltonians for the anisotropic interactions take the forms[33,34]

$$\bar{\tilde{H}}^{(1)}_{\sigma} = -\omega_0((R^{\sigma}_{0,0})^L T^{\sigma}_{0,0} + (R^{\sigma}_{2,0})^L T^{\sigma}_{2,0}) \quad (3)$$

$$\bar{\tilde{H}}^{(1)}_{Q} = \frac{2\pi C_Q}{2I(2I-1)}(R^{Q}_{2,0})^L T^{Q}_{2,0} \quad (4)$$

$$\bar{\tilde{H}}^{(2)}_{Q} = \frac{-\pi^2 C_Q{}^2}{2\omega_0 I^2(2I-1)^2}(2(R^{Q}_{2-})^L(R^{Q}_{2,1})^L[T^{Q}_{2,1}, T^{Q}_{2,-1}] + (R^{Q}_{2,-2})^L(R^{Q}_{2,2})^L[T^{Q}_{2,2}, T^{Q}_{2,-2}]) \quad (5)$$

where $\omega_0 = -\gamma B_0$ is the Larmor frequency and $C_Q = e^2qQ/h$ the quadrupole coupling constant.

The spin parts of the Hamiltonians are described by the irreducible tensor operators[35] $T^{\lambda}_{j,m}$ ($\lambda = \sigma$ or Q) of rank j included in Table 1. We note the relations

$$[T^{Q}_{2,1}, T^{Q}_{2,-1}] = \frac{1}{2}I_z(4I(I+1) - 8I_z{}^2 - 1) \quad (6)$$

$$[T^{Q}_{2,2}, T^{Q}_{2,-2}] = I_z(2I(I+1) - 2I_z{}^2 - 1) \quad (7)$$

Likewise, the spatial dependencies are expressed in the laboratory-fixed frame (L) by the irreducible tensors $(R^{\lambda}_{j,0})^L$. Among these $(R^{\sigma}_{0,0})^L = (R^{\sigma}_{0,0})^P$ is a scalar and the second-rank tensor element $(R^{\lambda}_{2,0})^L$ is related to the tensor elements $(R^{\lambda}_{j,m})^P$ in the principal-axis frame (P^λ) of the interaction λ (tensors included in Table 1) according to

$$(R^{\lambda}_{2,0})^L = \sum_{m=-2}^{2}\sum_{m'=-2}^{2}(R^{\lambda}_{2,m'})^P \mathbf{D}^{(2)}_{m',m}(\Omega^{\lambda}_{PC})\mathbf{D}^{(2)}_{m',0}(\Omega_{CL}) \quad (8)$$

where $D^{(2)}_{k,l}$ denotes the k,l element of the second-rank Wigner matrix[36] and $\Omega_{XY} = (\alpha_{XY}, \beta_{XY}, \gamma_{XY})$ Euler angles relating the coordinate systems X and Y. C refers to a crystal-fixed frame, which in this study for simplicity is chosen to be coincident with the principal-axis frame P^Q of the quadrupolar interaction (i.e., $\Omega^{Q}_{PC} = (0,0,0)$).

By use of the general Hamiltonian defined in eq 1, it is a straightforward matter to calculate the response of a powder of half-integer quadrupolar nuclei to the QCPMG pulse sequence

in Figure 1a. The propagator for the time evolution may conveniently be written

$$\tilde{U}_q(t_b,t_a) = \exp\{-i\int_{t_a}^{t_b}\bar{\tilde{H}}_q\,dt'\} = \exp\{-i\tilde{H}_q(t_b - t_a)\} \qquad (9)$$

where the subscript is used to distinguish between evolutions under Hamiltonians without rf irradiation (i.e., $\omega_{rf} = 0$) (q = f), with x-phase ($\phi = 0$) rf irradiation ($q = x$), or with y-phase ($\phi = \pi/2$) rf irradiation ($q = y$). For periods with free precession (q = f) the propagator is generated by straightforward exponentialization, since the Hamiltonian is diagonal. For periods with rf irradiation the propagator is formed using diagonalization, i.e.,

$$\tilde{U}_q(t_b,t_a) = D\,\exp\{-i\bar{\tilde{H}}_q^D(t_b - t_a)\}D^\dagger \quad q = x \text{ or } y \qquad (10)$$

where D represents a unitary transformation leading to the diagonalized Hamiltonian $\bar{\tilde{H}}_q^D = D^\dagger\,\bar{\tilde{H}}_q\,D$.

Considering the pulse scheme in Figure 1a, it is useful to introduce propagators describing the evolution during the initial QE sequence (part A) and the repeating echo sequence in part B (designated by subscripts A and B, respectively):

$$\tilde{U}_A^\dagger = \tilde{U}_x^\dagger(\tau_{\pi/2},0)\,\tilde{U}_f^\dagger(\tau_1,0)\,\tilde{U}_y^\dagger(\tau_\pi,0)\,\tilde{U}_f^\dagger\left(\tau_2 + \frac{\tau_a}{2},0\right) \qquad (11)$$

$$\tilde{U}_B^\dagger = \tilde{U}_f^\dagger(\tau_3,0)\,\tilde{U}_y^\dagger(\tau_\pi,0)\,\tilde{U}_f^\dagger(\tau_4,0)\,\tilde{U}_f^\dagger(\tau_a,0) \qquad (12)$$

where $\tau_{\pi/2}$ and τ_π denote widths of $\pi/2$ and π pulses. Now by introducing the periods

$$\tau_A = \tau_{\pi/2} + \tau_1 + \tau_\pi + \tau_2 + \frac{\tau_a}{2} \qquad (13)$$

$$\tau_B = \tau_3 + \tau_\pi + \tau_4 + \tau_a \qquad (14)$$

the propagator at any time $t_2 = t' + \Delta t$ with $t' = \tau_A - \tau_a/2$ for $M = 0$ and $t' = \tau_A + M\tau_B - \tau_a$ for $M > 0$ within the sampling period may be written

$$\tilde{U}^\dagger(t_2,0) = \begin{cases} \tilde{U}_A^\dagger\tilde{U}_f^\dagger\left(\frac{\tau_a}{2},0\right)\tilde{U}_f^\dagger(\Delta t,0), & \Delta t \in \left[0,\frac{\tau_a}{2}\right[, \text{ for } M = 0 \\ U_A^\dagger(\tilde{U}_B^\dagger)^M\tilde{U}^\dagger(t_a,0)\tilde{U}_f^\dagger(\Delta t,0), & \Delta t \in \left[0,\frac{\tau_a}{2}\right[, \text{ for } M > 0 \end{cases} \qquad (15)$$

with the upper limit τ_a replaced by $\tau_a + \tau_d$ for $M = N$, where N is the total number of π_y pulses. It should be noted that the apparent time scale of the sampled FID differs from the real time scale as illustrated in Figure 1b.

With the propagator in eq 15 at hand, the sampled FID for a powder sample may be calculated using

$$s(t_2) = \frac{1}{4\pi}\int_0^{2\pi}d\alpha_{CL}\int_0^{\pi}d\beta_{CL}\,\sin\beta_{CL}\,Tr\{I^+\,\tilde{U}\,(t_2,0)I_z\,\tilde{U}^\dagger(t_2,0)\} \qquad (16)$$

where we have taken the operators I_z and I^- as representatives of the initial and observable spin states, respectively, and averaged over all uniformly distributed crystallite orientations.

Qualitatively, the QCPMG pulse sequence in Figure 1a splits the QE spectrum, which would result from sampling of the decaying part of the first echo alone (i.e., part A of the pulse sequence), into a manifold of sidebands separated by $1/\tau_a$. Thus, the number and separation between the sidebands may be adjusted by changing the interpulse acquisition period τ_a. This partition of the powder spectrum into distinct sidebands leads to a considerable increase in the overall sensitivity of the experiment. In this and other respects the spin−echoes observed in QCPMG experiments resemble the rotational echoes observed in magic-angle spinning (MAS) experiments. Before experimental results that demonstrate the actual gain in sensitivity are presented it appears relevant first to discuss various aspects of numerical calculations based on the theory above. Furthermore, through numerical simulations we evaluate the capability of the method for accurate determination of parameters for the anisotropic inhomogeneous interactions.

3. Numerical Simulation and Iterative Fitting

On basis of eq 16 it is a straightforward matter to set up numerical simulation software for calculating the response of half-integer quadrupolar nuclei in a powder to the general QCPMG pulse sequence in Figure 1a. However, by use of an adequate number of uniformly distributed crystallite orientations in the powder averaging and by taking the effects of finite rf pulses into account, the numerical simulations may be rather time-consuming. Although this may not be an issue for a single simulation, it represents serious problems to QCPMG being a general method for determination of accurate values for the magnitudes and relative orientations of chemical shielding and quadrupole coupling tensors by iterative fitting of experimental spectra. Therefore, it appears relevant to address methods that reduce the computation time.

A. Tiling Schemes. A well-known obstacle in the calculation of NMR spectra for static powders is the very large number of crystallite orientations required for numerical powder averaging. Since the computer processing time is proportional to the number of crystallite orientations, it is crucial to use a powder averaging method that requires the lowest possible number of crystallite orientations for an acceptable powder averaging. Recently, it has been demonstrated[16] that selection of the crystallite orientations according to the tiling scheme of Zaremba,[37] Conroy,[38] and Wolfsberg and co-workers[39] leads to efficient powder averaging for a decently low number of crystallites. When this method is employed, the pairs of (α_{CL}, β_{CL}) crystallite angles are selected according to

$$\alpha = \frac{i}{N}2\pi,\ \beta = mod\left(\frac{ip_2}{N}\pi\right),\ i \in \{1, ..., N\} \qquad (17)$$

where *mod* denotes the decimal part of the fraction. The number N of crystallite orientations is a Fibonacci number and p_2 is the previous Fibonacci number. In this work all calculations employ $N = 17711$ and $p_2 = 10946$, which ensures convergence of the powder averaging.

B. Finite rf Pulses. Another important issue for the computation time is the potential need to include effects of finite rf pulses in the calculation. For the special case of ideal rf pulses (i.e., for $|\tilde{H}_{rf}| \gg |\tilde{H}_Q|, |\tilde{H}_\sigma|$), a dramatic reduction in the time for the calculation of the FID may be obtained. This is achieved by calculating the FID corresponding to a sequence with $M = 0$. From this half-echo envelope the full envelope may be generated ($M = 1$) and subsequently the total FID is formed by replicating the FID resulting from part B of the pulse sequence ($M = 1$) up to the desired number of points. For the typical case where $|\tilde{H}_{rf}|$ is less dominant, it is necessary to calculate the entire FID on the basis of eq 16. Figure 2 illustrates the effect of finite rf pulses on the appearance of the sideband envelope detected using the QCPMG pulse sequence. Specifically, the spectra are calculated for a powder of spin $I = 3/2$

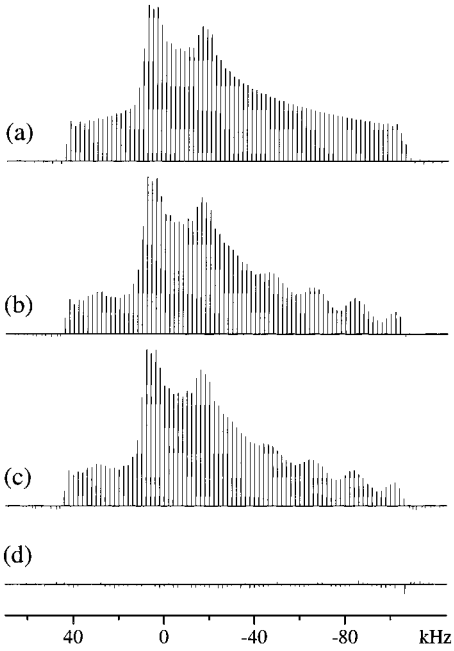

Figure 2. Theoretical QCPMG spectra ($I = 3/2$, $\omega_0/2\pi = -130.84$ MHz, $\sigma_{aniso} = -73.8$ ppm, $\eta_\sigma = 0.38$, $\Omega^\sigma_{CL} = (83°, 11°, 132°)$, $C_Q = 9.7$ MHz, and $\eta_Q = 0.72$) illustrating the effect of nonideal rf excitation. The spectrum in (a) is obtained using ideal (infinitely short) rf pulses by calculating the part of the FID corresponding to part A of the pulse sequence, reflecting this half echo to generate a full echo, which is replicated M times to form the remaining part B of the FID. Spectrum in (b) is calculated using eq 16 with finite rf pulse widths of $t_{\pi/2} = t_\pi/2 = 1.6$ μs corresponding to $\omega_{rf}/2\pi = -78.1$ kHz. The spectrum in (c) is calculated using the procedure leading to (b) with $M = 1$ and replicating part B of this FID to generate the full FID. The difference between the simulations in (b) and (c) is given in (d).

nuclei influenced by anisotropic chemical shielding ($\sigma_{aniso} = -73.8$ ppm, $\eta_\sigma = 0.38$) and quadrupolar coupling ($C_Q = 9.7$ MHz, $\eta_Q = 0.72$) interactions at $\omega_0/2\pi = -130.84$ MHz and exhibiting a relative tensor orientation defined by the Euler angles (α^σ_{PC}, β^σ_{PC}, γ^σ_{PC}) = (83°, 11°, 132°).

It is clear that the spectrum representing ideal rf excitation (infinitely short pulses) in Figure 2a differs significantly from the spectrum (Figure 2b) calculated using an experimentally typical rf field strength of $\omega_{rf}/2\pi = -78.125$ kHz (i.e., a selective $\pi/2$ pulse width $\tau_{\pi/2} = 1.6$ μs). Clearly, with the application of the QCPMG technique in mind, this difference implies that finite rf pulses must be taken into account in order to extract accurate values for the anisotropic interactions from experimental QCPMG spectra. Unfortunately, in the present example (for $M = 15$ cycles each representing 500 sampling points) this leads to an increase in the computation time by a factor of ca. 15, which makes iterative fitting an unwieldy procedure in cases of practical relevance. In an attempt to remedy this disadvantage, the spectrum in Figure 2c represents a combination of the two approaches used for the spectra in parts a and b of Figure 2. Specifically, the spectrum in Figure 2c is obtained by calculating the FID corresponding to the A and $M = 1$ B parts of the pulse sequence under assumption of finite rf pulses and then generating the remaining part of the FID by appending $M - 1$ replications of the $M = 1$ B part. The insignificant differences between the spectra in parts b and c of Figure 2 (see Figure 2d) indicate that the approximate procedure, employed in Figure 2c, may be of important value in the time-consuming part of the iterative fitting, since computation time is increased by a factor of only ca. 1.2 compared to the case of ideal pulses.

C. Homogeneous Interactions. As already addressed in the introductory part, other sources causing spectral distortions are homogeneous interactions such as molecular dynamics and homonuclear dipolar coupling. Both effects give rise to characteristic line shapes for the sidebands, which may be difficult to account for in the numerical simulations unless the actual perturbation is known. Even in such cases it may be undesirable to include these effects in the calculations, since they lead to a dramatic increase in the computation time. To circumvent this problem and to extract parameters for the inhomogeneous interactions, iterative fitting is based on integrated sideband intensities (i.e., stick plots).

***D.* Iterative Fitting.** A final issue to be concerned with in relation to the computational efforts involved in determining magnitudes and relative orientations of several anisotropic interactions from QCPMG spectra is the combination of the simulation program with efficient routines for numerical optimization and iterative fitting. Obviously, it is crucial to employ optimization procedures that are fast, insensitive to local minima, and capable of handling a large number of variables. Therefore, our simulation program has been combined with the CERN least-squares optimization package MINUIT,[40] which allows the use of appropriate combinations of Monte Carlo, simplex, and steepest-descent procedures in the minimization. Such combinations have proven very efficient for systematic optimization of solid-state NMR powder spectra that depend on several variables.[41,42]

4. Sensitivity of Parameters in Iterative Fitting of Spectra

The general applicability of the QCPMG method for determination of magnitudes and relative orientations of chemical shielding and quadrupolar coupling tensors highly depends on the intrinsic sensitivity of the method toward variations in the eight parameters C_Q, η_Q, σ_{iso}, σ_{aniso}, η_σ, α^σ_{PC}, β^σ_{PC}, and γ^σ_{PC}. Although the envelope of the QCPMG sideband spectrum closely resembles that of a standard QE spectrum, which may be analyzed in detail as previously described,[12−15,43] it appears relevant to briefly demonstrate the effect of variation in these parameters. Furthermore, these simulations may facilitate estimation of initial values for the parameters to be used in an iterative fitting. As an illustration, simulations are based on a parameters set for a powder of $I = 3/2$ nuclei with a resonance frequency $\omega_0/2\pi = -130$ MHz and a combination of anisotropic chemical shielding ($\sigma_{aniso} = 100$ ppm, $\eta_\sigma = 0.6$) and quadrupolar coupling ($C_Q = 5$ MHz, $\eta_Q = 0.3$) with a relative orientation of the two tensors given by $\Omega^\sigma_{PC} = (90°, 30°, 90°)$.

Figure 3 illustrates the dependence of the spectral appearance on variations for the quadrupole coupling parameters C_Q and η_Q. It is evident that when C_Q is increased from 2.5 to 10 MHz (parts a−d, the appearance of the QCPMG spectrum changes from a pattern resembling that of the chemical shielding anisotropy (CSA) to that being primarily dominated by the quadrupolar coupling interaction. The latter case represents a typical application for the QCPMG method, and an estimate of C_Q may be obtained from the total width of central transition powder pattern. According to the formulas of Baugher *et al.*,[43] C_Q may be estimated by employing

$$C_Q = 8I(2I-1)\sqrt{\frac{\omega_0 \Delta\nu}{2\pi\left(I(I+1)-\frac{3}{4}\right)(\eta_Q{}^2 + 22\eta_Q + 25)}} \quad (18)$$

where $\Delta\nu$ is the overall width (in frequency units) of the central (1/2, −1/2) transition and $0 \le \eta_Q \le 1$. An impression of the

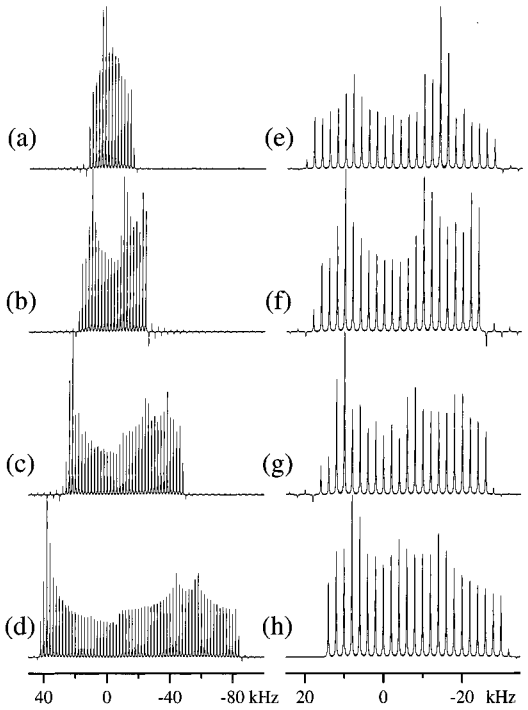

Figure 3. Simulated QCPMG spectra illustrating the dependence on C_Q (left column) and η_Q (right column). Parameters are $I = 3/2$, $\omega_0/2\pi = -130$ MHz, $\sigma_{iso} = 0$, $\sigma_{aniso} = 100$ ppm, $\eta_\sigma = 0.6$, and $\Omega^\sigma_{PC} = (90°, 30°, 90°)$. Parts a−d are with $\eta_Q = 0.3$ and $C_Q = 2.5$, 5.0, 7.5, and 10.0 MHz going from (a) to (d). Parts e−h are with $C_Q = 5.0$ MHz and $\eta_Q = 0.0$, 0.3, 0.6, and 0.9 going from (e) to (h).

sensitivity of the QCPMG spectra toward variation in η_Q is illustrated by the simulations in parts e−h of Figure 3.

The corresponding responses toward variation in the parameters σ_{aniso} and η_σ for the generally less dominant chemical shielding tensor are illustrated in Figure 4. In particular it should be noted that even in the regime of $|\bar{H}_Q \gg |\bar{H}_o|$ (illustrated by $\sigma_{aniso} \pm 10$ ppm in parts c and d of Figure 4), it should be possible to detect the influence of the CSA. Finally, the simulations in Figure 5 illustrate the effects of different relative orientations for the two tensors on the appearance of the QPCMG spectra. It is evident that variations in the Euler angle β^σ_{PC} (parts e−h cause the most pronounced changes in the sideband envelope, while the QCPMG spectra appear less sensitive to variations in the Euler angles α^σ_{PC} and γ^σ_{PC} parts a−d and i−l. We note that in the special cases of $\eta_\sigma = 0.0$ and $\eta_Q = 0.0$, the QCPMG spectrum (not shown) is independent of α^σ_{PC} and γ^σ_{PC}, respectively, observations also seen in MAS NMR of quadrupolar nuclei.[41]

5. Experimental Section

^{87}Rb (130.84 MHz) and ^{59}Co (94.43 MHz) experiments were performed on a Varian UNITY-400 NMR spectrometer (9.4 T) using a wideband Varian static-powder probe. For both nuclei an rf field strength of $\omega_{rf}/2\pi = -78$ kHz was employed. Considering the increase in effective nutation frequency by the factor $(I + 1/2)$ for the central $(1/2, -1/2)$ transition when $2\pi C_Q/(4I(2I - 1)\omega_{rf}) > 3$,[31,32] this corresponds to $\pi/2$-pulse widths of 1.6 μs for ^{87}Rb ($I = 3/2$) and 0.8 μs for ^{59}Co ($I = 7/2$). The rf field strengths were calibrated using 1.0 M $RbNO_3$ and 0.5 M $K_3Co(CN)_6$ aqueous solutions, which also served as external ^{87}Rb and ^{59}Co chemical shift references, respectively. The QCPMG spectra were recorded using the pulse sequence in Figure 1a and the phase cycle in Table 2. The standard QE experiments employed part A of the pulse sequence in Figure 1a with $\tau_a/2$ extended to record the full-echo decay and using the QE phase cycle also listed in Table 2. All calculations were performed on a Digital Alpha 1000 4/200 workstation. Typically, simulation of an $I = 3/2$ QCPMG spectrum employing finite rf pulses (see above), $M = 16$, a total number of 4256 points (256 points during a single τ_a period and 32 points during τ_d), and 17711 crystalline orientations required 42 s of CPU time. Considering the accumulative effect of finite rf pulses during all echo periods, a simulation required 5.8 min. $RbClO_4$ was purchased from Alpha Products and used without further purification. $RbVO_3$ was synthesized as described elsewhere.[45] $Co(NH_3)_5$ Cl_3 was a gift from from Kemisk Vørk Køge, Denmark.

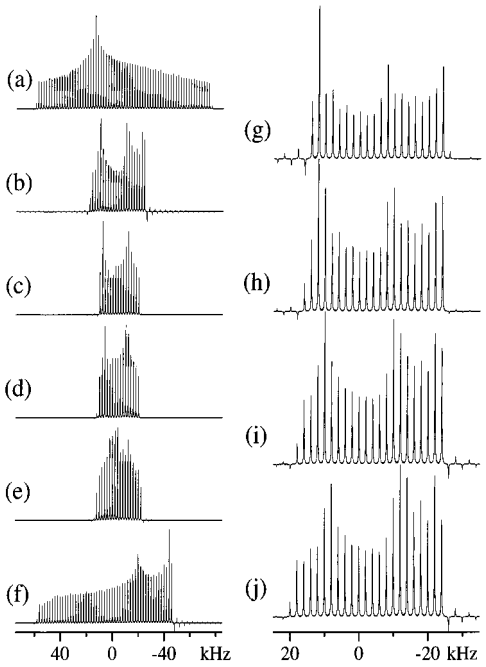

Figure 4. Theoretical QCPMG spectra displaying the dependence on σ_{aniso} (left column) and η_σ (right column). Parameters are $I = 3/2$, $\omega_0/2\pi = -130$ MHz, $C_Q = 5.0$ MHz, $\eta_Q = 0.3$, $\sigma_{iso} = 0$, and $(\alpha^\sigma_{PC}, \beta^\sigma_{PC}, \gamma^\sigma_{PC}) = (90°, 30°, 90°)$. Parts a−f are with $\eta_\sigma = 0.6$ and $\sigma_{aniso} = 500$, 100, 10, −10, −100, and −500 ppm going from (a) to (f). Parts g−j are with $\sigma_{aniso} = 100$ ppm and $\eta_\sigma = 0.0$, 0.3, 0.6, and 0.9 going from (g) to (j).

TABLE 2: Phase Cycles for the QE and the QCPMG Pulse Sequences[a]

QE			QCPMG[b]			
ϕ_1	ϕ_2	ϕ_{rec}	ϕ_1	ϕ_2	ϕ_3	ϕ_{rec}
x	y	$-x$	x	y	y	$-x$
$-x$	$-y$	x	y	x	x	$-y$
x	$-y$	$-x$	$-x$	y	y	x
$-x$	y	x	$-y$	x	x	y
y	$-x$	$-y$	x	$-y$	$-y$	$-x$
$-y$	$-x$	y	y	$-x$	$-x$	$-y$
y	x	$-y$	$-x$	$-y$	$-y$	x
$-y$	x	y	$-y$	$-x$	$-x$	y
x	y	$-x$	x	y	$-y$	$-x$
y	$-x$	$-y$	y	x	$-x$	$-y$
$-x$	$-y$	x	$-x$	y	$-y$	x
$-y$	x	y	$-y$	x	$-x$	y
x	$-y$	$-x$	x	$-y$	y	$-x$
y	x	$-y$	y	$-x$	x	$-y$
$-x$	y	x	$-x$	$-y$	y	x
$-y$	$-x$	y	$-y$	$-x$	x	y

[a] The pulse phases $\phi_1 - \phi_3$ corresponds to those in Figure 1a. ϕ_{rec} denotes the receiver reference phase. [b] The phase cycle is based on the first eight steps of the cycle proposed by Rance and Byrd.[44]

TABLE 3: Magnitudes and Relative Orientation of Quadrupolar Coupling and Chemical Shielding Tensors for ^{87}Rb in $RbClO_4$ and $RbVO_3$ and for ^{59}Co in $(Co(NH_3)_5\ Cl)Cl_2$ Determined by Iterative Fitting of QCPMG Powder Spectra[a]

compound	method	C_Q	η_Q	σ_{iso}[b]	σ_{aniso}	η_σ	α^σ_{PC}	β^σ_{PC}	γ^σ_{PC}	ref/figure
$RbClO_4$	SC	3.30	0.21	13.7	13.8	0.61	94	28	87	49
	QE	3.24	0.19	14.3	14.0	0.50	112	28.8	16	16
	MAS	3.29	0.20	13.1	13.5	0.32	98	34	69	51
	QCPMG	3.30	0.22	12.8	13.7	0.76	118	40	111	thiswork/7d
	QCPMG	3.28	0.24	12.4	13.0	1.00	118	32	97	thiswork/7h
	QCPMG	3.29 ± 0.08	0.24 ± 0.06	12.5 ± 1.5	14.2 ± 3.0	0.68 ± 0.25	117 ± 20	36 ± 10	93 ± 15	this work/71
$RbVO_3$	SC	9.70	0.74	31	−32	0.3	90	27	271	50
	QCPMG	9.64	0.66	29.3	−71.4	0.86	96	5	73	this work/9d
	QCPMG	9.47	0.68	27.9	−71.6	0.80	112	23	108	this work/9h
	QCPMG	9.74 ± 0.2	0.72 ± 0.03	32.7 ± 5	−73.8 ± 30	0.38 ± 0.4	83 ± 30	11 ± 10	132 ± 40	this work/9l
$(Co(NH_3)_5Cl)Cl_2$	QCPMG	26.9 ± 0.5	0.0 ± 0.1	8890 ± 5	1260 ± 30	0.08 ± 0.1	11 ± 20	8 ± 5	98 ± 20	this work/11d

[a] SC denotes single-crystal NMR. The quadrupole coupling constant (C_Q), isotropic and anisotropic chemical shifts (σ_{iso} and σ_{aniso}), and relative tensor orientations (α^σ_{PC}, β^σ_{PC}, γ^σ_{PC}) are given in MHz, ppm, and degrees (relative to the principal axis system of the quadrupolar coupling interaction, i.e., Ω^Q_{PC} = (0,0,0), respectively. [b] Isotropic chemical shifts (corrected for second-order quadrupolar induced shifts) on the σ-scale are referenced to 1.0 M $RbNO_3$ (^{87}Rb) and 0.5 M K_3 $Co(CN)_6$ (^{59}Co) solutions.

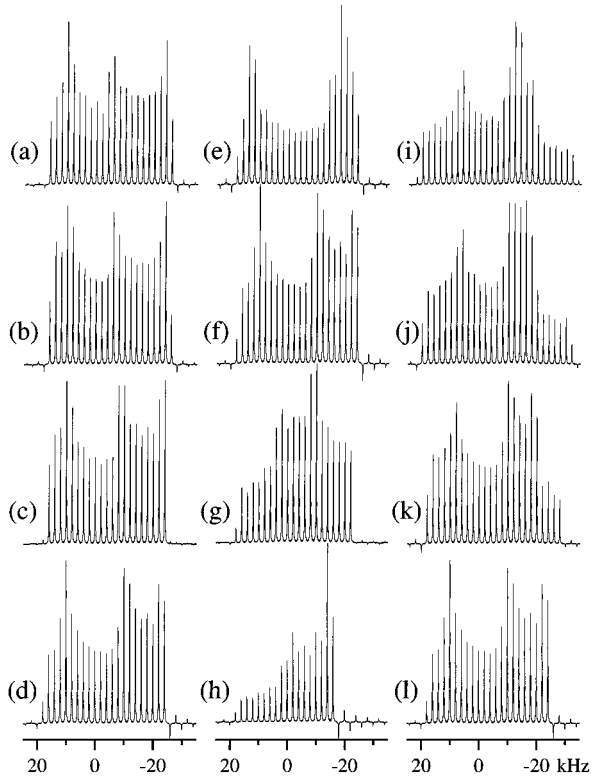

Figure 5. Calculated QCPMG spectra displaying the dependence on α^σ_{PC} (left column), β^σ_{PC} (middle column) and γ^σ_{PC} (right column). Parameters are I = 3/2, $\omega_0/2\pi$ = −130 MHz, C_Q = 5.0 MHz, η_Q = 0.3, σ_{iso} = 0, σ_{aniso} = 100 ppm, and η_σ = 0.6. Parts a−d are with (β^σ_{PC}, γ^σ_{PC}) = (30°, 90°) and α^σ_{PC} = 0°, 30°, 60°, 90° going from (a) to (d). Parts e−h are with (α^σ_{PC}, γ^σ_{PC}) = (90°, 90°) and β^σ_{PC} = 0°, 30°, 60°, 90° going from (e) to (h). Parts i−l are with (α^σ_{PC}, β^σ_{PC}) = (30°, 90°) and γ^σ_{PC} = 0°, 30°, 60°, 90° going from (i) to (l).

6. Results and Discussion

Applications of the QCPMG method for the determination of magnitudes and relative orientation of quadrupolar coupling and chemical shielding tensors by iterative fitting of integrated sideband intensities of experimental powder spectra are demonstrated in this section for ^{87}Rb in $RbClO_4$ and $RbVO_3$ and for ^{59}Co in $(Co(NH_3)_5\ Cl)Cl_2$. These samples have been chosen since they represent typical cases exhibiting different spin quantum numbers as well as magnitudes of the quadrupolar coupling and anisotropic chemical shielding interactions. The two rubidium salts have previously been investigated using static powder QE ($RbClO_4$,[16] $RbVO_3$[50]), single-crystal ($RbClO_4$,[49] $RbVO_3$[50]), and MAS ($RbClO_4$[51]) NMR while to our knowledge the cobalt complex has not previously been studied. To appreciate the sensitivity gain and the accuracy of the parameters determined by iterative fitting, QCPMG spectra with different sideband separations and standard QE spectra have been recorded and analyzed for all samples.

In the analysis and interpretation of the relative orientation of the principal axis systems for the quadrupole coupling and chemical shielding tensors, it is essential that potential effects of crystal symmetry (i.e., space group symmetry) is considered. Since the two tensors are invariant toward symmetry operations within the space group, crystal symmetry imposes certain restrictions on the Euler angles Ω^σ_{PC} relating the two tensors. X-ray diffraction (XRD) studies show that $RbClO_4$,[46] $RbVO_3$,[47] and $(Co(NH_3)_5\ Cl)Cl_2$[48] all have orthorhombic crystal structure with space groups *Pnma*, *Pbcm*, and *Pnma*, respectively. These space groups all exhibit a mirror or a C_2 axis at the positions of the quadrupolar nuclei of interest in the crystal lattice of these compounds. The mirror plane symmetry requires that the quadrupole coupling and the chemical shielding tensors both have one principal axis perpendicular to this plane.[13,49−52] This implies that the angles α^σ_{PC} and γ^σ_{PC} are a multiple of 90° but not necessarily the same multiple.

Parameters describing the magnitudes and relative orientation of the quadrupole coupling and chemical shielding tensors determined here and elsewhere for the three samples are summarized in Table 3.

A. $RbClO_4$. Figure 6 shows typical ^{87}Rb NMR spectra of $RbClO_4$ recorded using the QCPMG experiment for different τ_a values (corresponding to different sideband separations) along with the conventional QE spectrum. Clearly, the QCPMG technique splits the static-powder spectrum of the QE experiment (Figure 6d) into a manifold of sidebands that exhibit an envelope quite similar to that of the QE spectrum. Depending on the number of sidebands, this gives a significant sensitivity enhancement as illustrated by the QCPMG spectra in parts a−c of Figure 6. These spectra show signal enhancement factors of 10.9, 4.4, and 2.2 compared to the QE spectrum.

To extract accurate parameters describing the magnitudes and relative orientations of the quadrupole coupling and chemical shielding tensors, the QCPMG and QE spectra were simulated and iteratively fitted by employing a computer program based on the principles given above. The resulting optimized simulated spectra are shown in Figure 7 (parts d, h, and l in the lower row) for comparison with the corresponding experimental spectra in the top row. The optimized parameters corresponding to the three simulated QCPMG spectra are summarized in Table 3 and may be compared with the parameters determined from previous studies.[16,49,51]

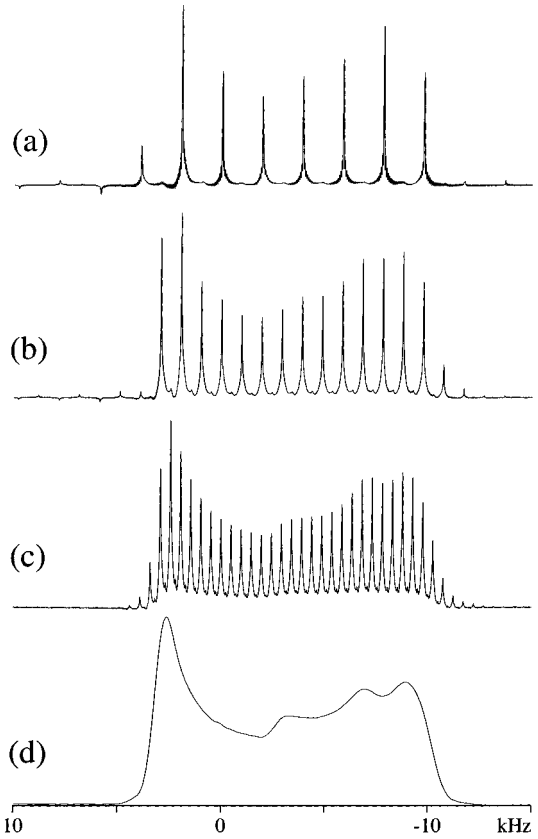

Figure 6. Experimental ^{87}Rb (130.84 MHz) QCPMG (a−c) and QE (d) spectra of $RbClO_4$. The QCPMG spectra used the pulse sequence in Figure 1a with $\tau_1 = 25\ \mu$s, $\tau_2 = \tau_3 = 26\ \mu$s, $\tau_4 = 27\ \mu$s, 4 s relaxation delay, and a spectral width of 250 kHz. The number of echo periods M, number of scans, τ_a, and τ_d were (a) 60, 1024, 512 μs, and 128 μs, (b) 32, 3072, 1024 μs, and 256 μs, (c) 15, 8192, 2 ms, and 1.768 ms. The QE spectrum (d) employed 4096 scans and the same spectral width, τ_1, τ_2, and relaxation delay values as in (a−c). All spectra were weighted by a Lorentzian of 1 Hz line width. The vertical scale of the QCPMG spectra relative to the QE spectrum (d) were reduced by factors of 10.9, 4.4, 2.2 going from (a) to (c).

At this point it seems appropriate to specify the procedure used for iterative fitting. First, to ensure least-squares fitting to pure inhomogeneous contributions of the spin dynamics characterizing the experimental spectrum, our program compares integrated experimental and simulated sideband intensities as exemplified by the stick-plots in the second (experimental) and third (simulated) rows of Figure 7. Second, to facilitate the seven-parameter fit, the starting value for C_Q can be estimated to fall in the range 2.8−3.9 MHz using eq 18 with $\Delta\nu = 15$ kHz. Furthermore, the sideband envelope indicates that the spectrum is dominated by the quadrupolar interaction and $\eta_Q \simeq 0.2-0.4$. By use of these parameters as a start, iterative fitting of the experimental "stick-plot" intensities gives the optimized parameters in Table 3, the corresponding simulated stick-plot spectra in Figure 7 (third row), and the line-shape-simulated QCPMG spectra in the bottom row.

Comparison of the spectra in Figure 7 reveals a reasonable agreement between experimental and calculated stick-plot spectra for the three QCPMG experiments representing different sampling conditions. Apart from minor differences near the baseline, a similar agreement is observed for the spectra including line shape. This shows that the experimental spectra, to a good approximation, reflect purely inhomogeneous interactions (chemical shielding and quadrupole coupling), while homogeneous interactions from homonuclear dipolar coupling or dynamics play an insignificant role for ^{87}Rb in $RbClO_4$.

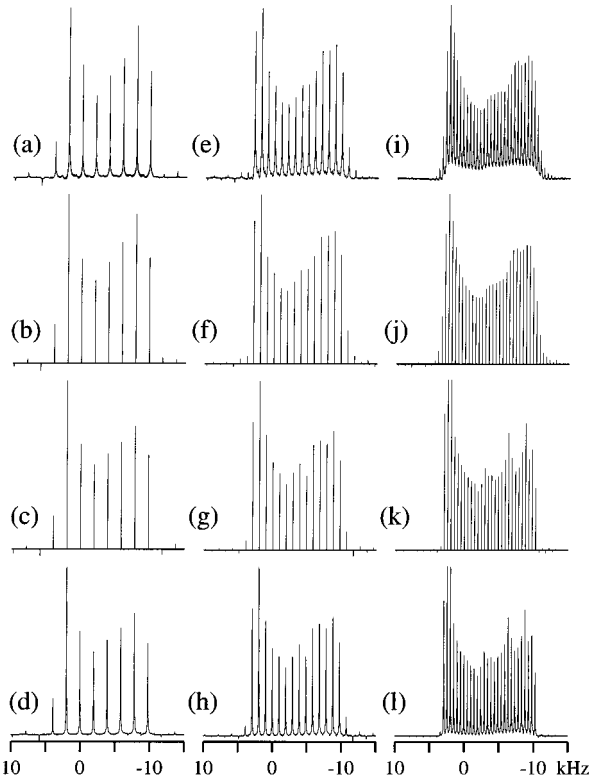

Figure 7. Experimental and optimum simulated ^{87}Rb QCPMG spectra of $RbClO_4$ corresponding to the pulse sequence parameters described in Figure 6a (left column), 6b (center column), and 6c (right column) and the interaction parameters given in Table 3. The full experimental, stick-plot of experimental sideband intensities, stick-plot of simulated sideband intensities, and full simulated spectra are reproduced in the first (a, e, i), second (b, f, j), third (c, g, k), and fourth (d, h, l) row.

Inspection of the three parameter sets determined for $RbClO_4$ (Table 3) shows small variations among the parameters even for the spectrum with few sidebands. This indicates that the sensitivity of the QE experiment may be increased by at least an order of magnitude by QCPMG without severely sacrificing the information content of the experiment and the accuracy of the parameters extracted. This advantage is similar to that observed in a comparison of standard MAS and static-powder NMR spectra. Comparison of the QCPMG parameters with those of the QE spectrum (Figure 6d) and previously determined data from single-crystal,[49] static-powder QE,[16] and MAS[51] NMR studies shows an excellent agreement for all parameters except for η_σ (determined with considerable uncertainty in all studies) and the value for γ^σ_{PC} determined from the QE spectrum by Koons et al.[16] and commented on previously. Accuracies estimated by numerical calculation and by visual inspection are given in Table 3 for the spectrum in Figure 7l. Similar accuracies may be determined from the other QCPMG spectra. It is noted that the α^σ_{PC} and γ^σ_{PC} values determined by QCPMG are fairly close to 90° (a value in agreement with crystal symmetry (vide supra).

B. $RbVO_3$. To demonstrate the sensitivity gain achieved by QCPMG relative to conventional QE for the important cases of broad anisotropic powder patterns, Figure 8 shows a series of ^{87}Rb QCPMG and QE spectra for $RbVO_3$. In accordance with a quadrupole coupling constant on the order of 10 MHz,[50] the second-order quadrupolar and CSA broadened powder pattern for the central (1/2, −1/2) transition extends over a frequency range of about 150 kHz. In addition to the large quadrupolar interaction, rendering static-powder QE NMR a relatively insensitive method, this compound represents an

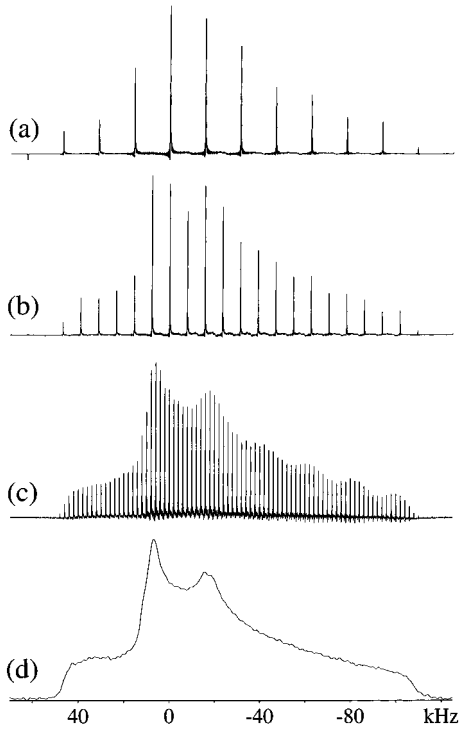

Figure 8. Experimental ^{87}Rb (130.84 MHz) QCPMG (a−c) and QE (d) spectra of $RbVO_3$. All QCPMG spectra were recorded using $\tau_1 = 25\ \mu s$, $\tau_2 = 25.8\ \mu s$, $\tau_3 = 26\ \mu s$, $\tau_4 = 26.8\ \mu s$, and 4 s relaxation delay. The individual spectra used spectral width, number of echo periods M, number of scans, τ_a, τ_d, and Lorentzian line broadening: (a) 2 MHz, 61, 1024, 64 μs, 159 μs, and 100 Hz; (b) 1 MHz, 62, 384, 128 μs, 190 μs, 50 Hz; (c) 1 MHz, 15, 4096, 500 μs, 440 μs, and 1 Hz. The QE spectrum was obtained using 2048 scans, $\tau_1 = 25\ \mu s$, $\tau_2 = 24.8\ \mu s$, 2 s relaxation delay, a 2 MHz spectral window, and a Lorentzian line broadening of 1 Hz. The intensity of the QCPMG spectra compared to the QE spectrum are 28.3, 12.7, 4.13, and 1.0 going from the top to the bottom spectrum (see text).

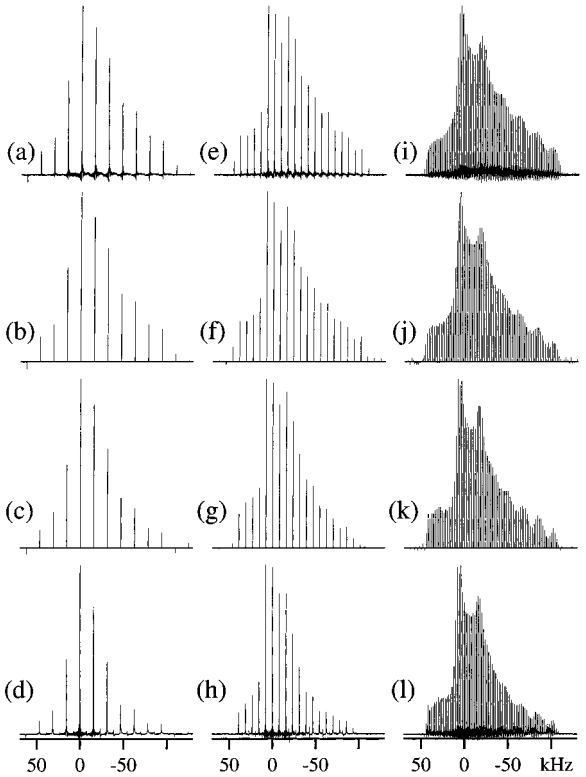

Figure 9. Comparison of experimental and optimum simulated ^{87}Rb QCPMG spectra of $RbVO_3$ corresponding to the experimental spectra and parameters given in Figure 8a (left column), 8b (middle column), 8c (rigth column) and the interaction parameters given in Table 3. The first, second, third, and fourth rows give full experimental (a, e, i), stick-plot of experimental sideband intensities (b, f, j), stick-plot of simulated sideband intensities (c, g, k), and full simulated spectra (d, h, l), respectively. The last spectra were apodized using a 50 Hz wide Lorentzian.

intriguing test for the QCPMG technique because of its rather small chemical shielding interaction.

The three QCPMG spectra in parts a−c of Figure 8 recorded using τ_a values adjusted to split the powder pattern into sidebands separated by 15.6, 7.8, and 2 kHz, display an intensity gain by factors of 28.3, 12.7, and 4.1, respectively, relative to the QE spectrum (Figure 8d). These numbers correspond to experiments using a spectral width of 2 MHz for the spectra in parts a and d of Figure 8 and 1 MHz for the spectra in parts b and c. In turn, this implies that the corresponding QCPMG experiments with 7.8 and 2 kHz sideband separation (corresponding to those in parts b and c of Figure 8) recorded using twice the spectral width would lead to gain factors of about 15 and 8, respectively. Furthermore, it is noted that the spectra in parts a and b of Figure 8 was apodized using Lorentzian line broadenings of 100 and 50 Hz, respectively, to avoid sinc wiggles by truncation of the FID. The spectrum in Figure 8c used 1 Hz line broadening, while 100 Hz was used for the spectrum in Figure 8d. Using a line broadening of 1 Hz and a spectral window of 2 MHz for all spectra leads to gain factors of about 46, 21, and 8 for the three spectra in parts a−c of Figure 8.

By employment of a quadrupole coupling constant in the range 9.2−12.7 kHz, estimated using eq 18 with $\Delta\nu = 160$ kHz, seven-parameter iterative fitting of the experimental QCPMG and QE spectra in Figure 8 leads to the parameters summarized in Table 3. For comparison Table 3 also includes the results from a recent single-crystal NMR study.[50] Figure 9 shows the experimental spectra, experimental stick-plots of sideband intensities, optimized fitted stick-plots of calculated sideband intensities, and optimized simulated spectra for all three QCPMG experiments. Comparison of the experimental and optimum simulated ^{87}Rb QCPMG spectra corresponding to different sideband separations demonstrates a good agreement with respect to both sideband intensities and line shapes over the entire spectral width. However, we note that slightly lower sideband intensities are observed in the high-field region of the calculated spectra compared to the experimental spectra. From the narrow lines observed in all experimental spectra (and reproduced in the simulated spectra) we conclude that homogeneous interactions contribute insignificantly to the spin dynamics of ^{87}Rb in $RbVO_3$.

Mutual comparison of the parameters determined by iterative fitting of the QCPMG and QE spectra (estimated accuracies included in Table 3 for the spectrum in Figure 9l) and against those determined previously by single-crystal NMR leads to the following observations. First, for the quadrupole coupling interaction all studies give almost identical C_Q and η_Q values within experimental error. Second, more uncertainty concerns the magnitude of the chemical shielding tensor, where the QCPMG and QE results predict $\sigma_{aniso} \simeq -72$ ppm compared to the value of -43 ppm determined by single-crystal NMR.[49] Likewise, the η_σ parameter is subjected to quite some uncertainty, since values in the range 0.3−0.8 are obtained. Third, although at first glance insensitive to the isotropic chemical shift by sampling under influence of refocusing pulses, the QCPMG experiments lead to isotropic chemical shift values (σ_{iso}) close to the value determined by single-crystal NMR. Fourth, for the relative orientation of the two tensorial interactions (specified

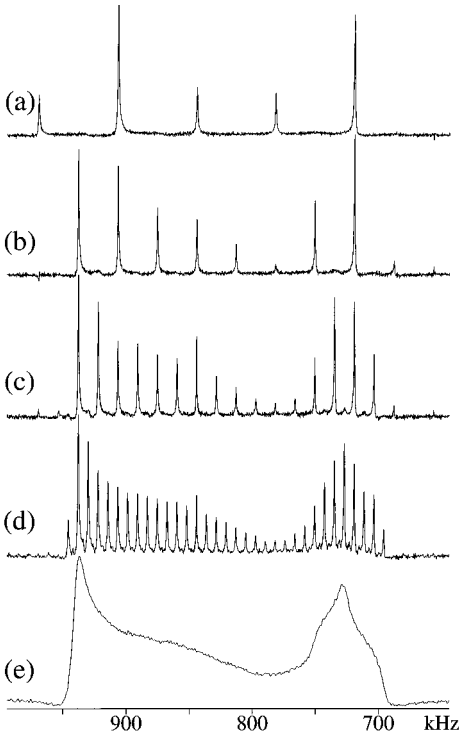

Figure 10. Experimental ^{59}Co (94.43 MHz) QCPMG (a−d), and QE (e) spectra of $(Co(NH_3)_5Cl)Cl_2$. The QCPMG spectra were recorded using the pulse sequence in Figure 1a with $\tau_1 = 25$ μs, $\tau_2 = \tau_3 = 26$ μs, $\tau_4 = 27$ μs, 4 s relaxation delay, and a dwell time of 0.5 μs (corresponding to a spectral width of 2 MHz). All spectra were processed using 1 Hz Lorentzian line broadening. For the QCPMG spectra the number of echo periods M, number of scans, τ_a, and τ_d were 128, 512, 16 μs, and 199 μs, (b) 63, 512, 32 μs, and 191 μs, (c) 61, 1024, 64 μs, and 159 μs, (d) 30, 2048, 128 μs, and $\tau_d = 191$ μs. The QE spectrum employed $\tau_1 = 25$ μs, $\tau_2 = 24$ μs, a relaxation delay of 2 s, 20 480 scans, and a spectral width of 2 MHz. The absolute intensity of the QCPMG spectra relative to the QE spectrum are 9.4, 7.3, 4.8, and 2.6 on going from (a) to (d).

by Ω^{σ}_{PC}), the QCPMG and QE results suggest α^{σ}_{PC} and γ^{σ}_{PC} both to be in the vicinity of 90° in accordance with crystal symmetry. This agrees well with the single-crystal NMR results,[50] which favor $\alpha^{\sigma}_{PC} = 90°$ and $\gamma^{\sigma}_{PC} \simeq -90°$, compatible with the *Pbcm* space group. Finally, considering the parameters overall, a comparison reveals that iterative fitting of the QCPMG spectrum with the smallest sideband separation generally leads to parameters closest to those determined by single-crystal NMR. However, quite similar results are obtained from QCPMG with larger sideband separations.

C. $(Co(NH_3)_5Cl)Cl_2$. As a final demonstration of sensitivity-enhanced QE NMR for a nucleus exhibiting a larger spin quantum number, Figure 10 shows a series of ^{59}Co ($I = 7/2$) QCPMG and QE NMR spectra of $(Co(NH_3)_5Cl)Cl_2$. The four QCPMG spectra were recorded with τ_a adjusted to split the 270 kHz wide second-order quadrupolar coupling and CSA broadened central-transition powder pattern into a manifold of spin−echo sidebands with separations of 62.5, 31.3, 15.6, and 7.8 kHz. The envelope of the sideband manifold in all spectra exhibits clear similarities to the QE spectrum (Figure 10e). Comparison of the signal intensities of the QCPMG relative to the QE spectra reveals intensity enhancements by factors of 9.4, 7.3, 4.8, and 2.6 on going from the spectrum with the largest to the smallest sideband separation.

The envelope of the spin−echo sideband manifold indicates the presence of large quadrupolar coupling *and* anisotropic chemical shielding interactions for ^{59}Co in this compound. Considering the quadrupole interaction alone, the width of the central transition (270 kHz) suggests C_Q to be in the range 31−44 MHz. A more detailed determination of the parameters for the two anisotropic interactions requires iterative fitting of the experimental spectra in Figure 10, although we note that the calculations due to a larger matrix dimension are a factor of 8 slower than the corresponding $I = 3/2$ calculations performed above. For this reason, we restrict the analysis to the experimental QCPMG spectrum in Figure 10e. For this particular QCPMG experiment, Figure 11 compares the experimental and optimum simulated spectra, while Table 3 gives the corresponding optimum parameters and their estimated accuracies. Although the agreement between the experimental and simulated spectra is less favorable than observed for the ^{87}Rb spectra above, Table 3 clearly reinforces the presence of large quadrupolar coupling and anisotropic shielding interactions. Furthermore, it is noted that the optimum values for α^{σ}_{PC} and γ^{σ}_{PC} (close to 0° and 90°) are in accordance with the crystal symmetry (space group *Pnma*) for $(Co(NH_3)_5Cl)Cl_2$.

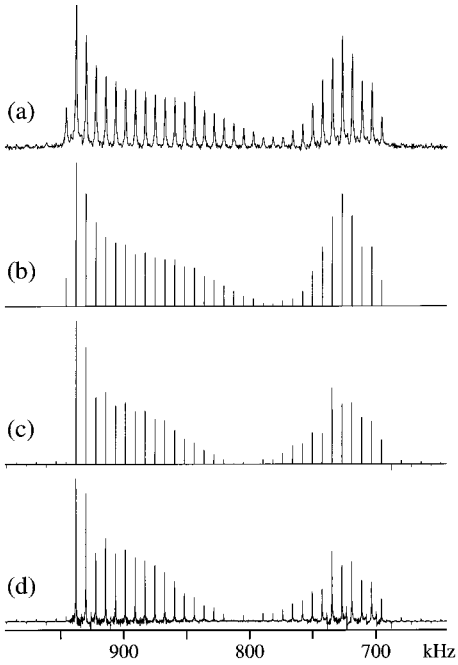

Figure 11. Comparison of experimental and optimum simulated ^{59}Co QCPMG spectra of $(Co(NH_3)_5Cl)Cl_2$: (a) experimental spectrum corresponding to Figure 10d and (b) stick-plot of experimental sideband intensities; (d) optimum simulated QCPMG spectrum and stick-plot of calculated sideband intensities (c) corresponding to the experimental parameters given in the caption of Figure 10 and the interaction parameters in Table 3.

7. Conclusions

In conclusion, we have introduced and demonstrated a new experimental method, QCPMG, for determination of magnitudes and relative orientation of chemical shielding and quadrupolar coupling tensors of half-integer quadrupolar nuclei exhibiting relatively large quadrupole coupling and anisotropic chemical shielding interactions. The method bears close resemblance to the conventional QE method but amplifies the sensitivity of this experiment significantly by recording the FID through a train of selective π refocusing pulses. In practical application to wide central-transition (1/2, −1/2) powder patterns, this may lead to a gain in sensitivity by a factor of say 30 as demonstrated in this study for quadrupolar nuclei characterized by 150−250 kHz wide line shapes. In combination with efficient computer software for simulation and iterative fitting of experimental to calculated sideband intensities, the method proves useful for

accurate determination of parameters for quadrupole coupling and chemical shielding tensors in polycrystalline solids. Currently, we are exploring combinations of QCPMG with MAS experiments.

Acknowledgment. The use of the Varian UNITY-400 NMR spectrometer, sponsored by Teknologistyrelsen, at the University of Aarhus Instrument Centre for Solid-State NMR Spectroscopy is acknowledged. Support of this research by equipment grants from the Danish Natural Science Research Council, Carlsbergfondet, and Aarhus University Research Foundation is acknowledged. This work was supported in part by the National Institutes of Health under a Related Services Agreement with the U.S. Department of Energy (DOE) under Contract DE-AC06-76RLS 1830, Federal Grant 8-R1GM26295F. Pacific Northwest National Laboratory is operated for DOE by Battelle.

References and Notes

(1) Solomon, I. *Phys. Rev.* **1958**, *110*, 61.
(2) Weisman, I. D.; Bennett, L. H. *Phys. Rev.* **1969**, *181*, 1341.
(3) Davis, J. H.; Jeffrey, K. R.; Bloom, M.; Valic, M. I.; Higgs, T. P. *Chem. Phys. Lett.* **1976**, *42*, 390.
(4) Hahn, E. L. *Phys. Rev.* **1950**, *80*, 580.
(5) Spiess, H. W. *Chem. Phys.* **1976**, *6*, 217.
(6) Hentschel, D.; Sillescu, H.; Spiess, H. W. *Polymer* **1984**, *25*, 1078.
(7) Griffin, R. G. *Methods Enzymol.* **1981**, *72*, 108.
(8) Barbara, T. M.; Greenfield, M. S.; Vold, R. L.; Vold, R. R. *J. Magn. Reson.* **1986**, *69*, 311.
(9) Vega, A. J.; Luz, Z. *J. Chem. Phys.*, **1987**, *86*, 1803.
(10) Kennedy, M. A.; Vold, R. R.; Vold, R. L. *J. Magn. Reson.*, **1991**, *91*, 301.
(11) Wittebort, R. J.; Olejniczak, E. T.; Griffin, R. G. *J. Chem. Phys.* **1987**, *86*, 5411.
(12) Cheng, J. T.; Edwards, J. C.; Ellis, P. D. *J. Phys. Chem.* **1990**, *94*, 553.
(13) Power, W. P.; Wasylishen, R. E.; Mooibroek, S.; Pettitt, B. A.; Danchura, D. *J. Phys. Chem.* **1990**, *94*, 591.
(14) Hirschinger, J.; Granger, P.; Rosé, J. *J. Phys. Chem.* **1992**, *96*, 4815.
(15) Chung, S. C.; Chan, C. C.; Au-Yeng, C. F.; Xu, X. *J. Phys. Chem.* **1993**, *97*, 12685.
(16) Koons, J. M.; Hughes, E.; Cho, H. M.; Ellis, P. D. *J. Magn. Reson. A* **1995**, *114*, 12. There was an error in the code of the program used in this paper. This has been corrected and the PNNL program now agrees with the results obtained in this paper.
(17) Carr, H. Y.; Purcell, E. M. *Phys. Rev.* **1954**, *94*, 630.
(18) Meiboom, S.; Gill, D. *Rev. Sci. Instrum.* **1958**, *29*, 688.
(19) Maricq, M. M.; Waugh, J. S. *J. Chem. Phys.* **1979**, *70*, 3300.
(20) Garroway, A. N. *J. Magn. Reson.* **1977**, *28*, 365.
(21) Vega, A. J. *J. Magn. Reson.* **1985**, *65*, 252.
(22) Swanson, S.; Ganapathy, S.; Kennedy, S.; Henrichs, P. M.; Bryant, R. G. *J. Magn. Reson.* **1986**, *69*, 531.
(23) Bloom, M.; Sternin, E. *Biochemistry* **1987**, *26*, 2101.
(24) Engelsberg, M.; Yannoni, C. S. *J. Magn. Reson.* **1990**, *88*, 393.
(25) Müeller, K.; Poupko, R.; Luz, Z. *J. Magn. Reson.* **1990**, *90*, 19.
(26) Lizak, M. J.; Gullion, T.; Conradi, M. S. *J. Magn. Reson.* **1991**, *91*, 254.
(27) Marchetti, P. S.; Bhattacharyya, L.; Ellis, P. D.; Brewer, C. F. *J. Magn. Reson.* **1988**, *80*, 417.
(28) Bank, S.; Bank, J. F.; Ellis, P. D. *J. Phys. Chem.* **1989**, *93*, 4847.
(29) Cheng, J. T.; Ellis, P. D. *J. Phys. Chem.* **1989**, *93*, 2549.
(30) Henrichs, P. M.; Nicely, V. A. *Macromolecules* **1991**, *24*, 2506.
(31) Abragam, A. *The Principles of Nuclear Magnetism*; Clarendon Press: Oxford, 1961.
(32) Schmidt, V. H. in *Proceedings Ampère International Summer School II*; Baško Polje, Yugoslavia, 1971; p 79.
(33) Samoson, A.; Kundla, E.; Lippmaa, E. *J. Magn. Reson.* **1982**, *49*, 350.
(34) Freude, D.; Haase, J. *NMR: Basic Princ. Prog.* **1993**, *29*, 1.
(35) Mehring, M. in *High Resolution NMR in Solids*, 2nd ed.; Springer: Berlin, 1983.
(36) Spiess, H. W. In *NMR Basic Principles and Progress*; Diehl, P., Fluck, E., Kosfeld, E. Eds.; Springer: Berlin, 1978.
(37) Zaremba, S. K. *Ann. Matematica Pura Appl.* **1966**, *73*, 293.
(38) Conroy, H. *J. Chem. Phys.* **1967**, *47*, 5307.
(39) Cheng, V. B.; Suzukava, H. H., Jr.; Wolfsberg, M. *J. Chem. Phys.* **1973**, *59*, 3992.
(40) James, F.; Ross, M. MINUIT computer code, CERN, Geneva Program D-506. *Comput. Phys. Commun.* **1975**, *10*, 343.
(41) Skibsted, J.; Nielsen, N. C.; Bildsøe, H.; Jakobsen, H. J. *Chem. Phys. Lett.* **1992**, *188*, 405.
(42) Skibsted, J.; Nielsen, N. C.; Bildsøe, H.; Jakobsen, H. J. *J. Am. Chem. Soc.* **1993**, *188*, 405.
(43) Baugher, J. F.; Taylor, P. C.; Oja, T.; Bray, P. J. *J. Chem. Phys.* **1969**, *115*, 7351.
(44) Rance, M.; Byrd, A. *J. Magn. Reson.* **1983**, *52*, 221.
(45) Feigelson, R. S.; Marin, G. W.; Johnson, B. C. *J. Cryst. Growth* **1972**, *13/14*, 686.
(46) Granzin, J. *Z. Kristallogr.* **1988**, *184*, 157.
(47) Hawthorne, F. C.; Calvo, C. *J. Solid State Chem.* **1977**, *22*, 157.
(48) Messmer, G. G.; Amma, E. L. *Acta Crystallogr.* **1968**, *B24*, 417.
(49) Vosegaard, T.; Skibsted, J.; Bildsøe, H.; Jakobsen, H. J. *J. Magn. Reson. A* **1996**, *122*, 111.
(50) Vosegaard, T.; Skibsted, J.; Bildsøe, H.; Jakobsen, H. J. In preparation.
(51) Vosegaard, T.; Skibsted, J.; Bildsøe, H.; Jakobsen, H. J. *J. Phys. Chem.* **1995**, *99*, 10731.
(52) Weil, J. A.; Buch, T.; Clapp, J. E. *Adv. Magn. Reson.* **1973**, *8*, 183.